Earth and Planetary Science Letters 304 (2011) 577–586

Contents lists available at ScienceDirect

Earth and Planetary Science Letters

journal homepage: www.elsevier.com/locate/epsl

Heat partitioning in metal-silicate plumes during Earth differentiation

Christina King *, Peter Olson

Department of Earth and Planetary Sciences, Johns Hopkins University, Baltimore, MD 21218, USA

ARTICLE INFO

Article history:
Received 18 October 2010
Received in revised form 16 February 2011
Accepted 18 February 2011

Editor: T. Spohn

Keywords:
core formation
metal-silicate plumes
viscous dissipation
diapirs
conduits
Earth's core

ABSTRACT

We present an analytical model for core formation that includes both metal diapirs and liquid conduits and produces a superheated core. We start from the standard model of Earth formation consisting of accretion by planetesimal or planetary embryo impacts large enough to create global or local magma oceans. Our model consists of two main fluid dynamical structures: 1) large liquid metal diapirs and 2) narrow conduits with liquid silicate and small liquid metal droplets. We assume that transport of metal from a near-surface magma ocean to the growing core occurs within these structures. The release of gravitational potential energy from the descent of the metal is converted to heat through viscous dissipation, which is broadly distributed around the large liquid metal diapirs but localized in the conduit around the smaller metal droplets. This model gives an average core temperature during accretion and a post-accretion average core temperature for a broad range of impact histories and chemical quilibration assumptions. We consider three types of Earth accretion histories with impacts that are evenly spaced over 30 Ma. These include: 1) equal-sized impacts, 2) equal-sized impacts with a final Mars-sized impact, and 3) exponentially decreasing impact sizes with a final Mars-sized impact. Our preferred model is based on core–mantle chemical equilibrium estimates that correspond to a fractionation, f, the ratio of metal in the diapir to the total metal content in each impact of $f = 0.64$ and accretion history type 3. This model produces a post-accretion average core temperature that ranges from 5930 K to 5700 K for 8 to 90 impacts, respectively. The efficiency of the metal-silicate conduits, defined as the ratio of the heating of the core by the conduits to their potential energy released has an approximate value of 0.59 for our preferred model. The residual post-accretion structures include a basal magma ocean and a network of mantle conduits that may dictate the style of Hadean tectonics.

1. Introduction

The abundances present today in the mantle of short-lived decay products such as ^{27}Mg and ^{182}W relative to non-radiogenic isotopes suggest that Earth differentiated during accretion over 30–40 Ma time, with most of its mass accreting within about 10 Ma and fully accreted by 100 Ma (Halliday, 2008; Halliday and Wood, 2007; Walter and Tronnes, 2004; Wood et al., 2006). Based on SPH simulations, a large Mars-sized impact is thought to have occurred at the end of the accretion of the Earth resulting in the moon formation (Canup, 2004), a key process in this study. Although it is widely thought that core formation took place during accretion, rather than later on, there are relatively few constraints on how the core formed.

Consideration of the physical processes by which the Earth accreted offers one approach to this question. The current paradigm for Earth accretion emphasizes the importance of large impact events (Canup, 2004; Halliday, 2008; Rudge et al., 2010; Tonks and Melosh, 1993; Wood et al., 2006). It is likely that many of these impact events involved massive, already differentiated projectiles that released enough kinetic and potential energy to produce substantial melting of both the projectile and the target, creating localized and possibly global magma oceans (Albarede, 2009; Corgne et al., 2008; Halliday, 2008; Pahlevan and Stevenson, 2007; Rudge et al., 2010; Tonks and Melosh, 1993; Walter and Tronnes, 2004). Parts of the already existing planetesimal proto-cores become fragmented during impact while other portions of the proto-core stay coherent and sink to the bottom of the magma ocean quickly. Once a large mass of metal reaches the bottom of the magma ocean it sinks through the solid mantle in the form of a large liquid diapir.

In a magma ocean environment, both metal-silicate segregation and equilibration processes occur on much shorter time scales than normally found under sub solidus conditions (Halliday and Wood, 2007). In particular, the processes of chemical and thermal equilibration between metal that is disseminated by impacts and silicates are greatly accelerated if the metal phase is finely dispersed, on the scale of droplets for example (Höink et al., 2006). Theory (Dahl and Stevenson, 2010) predicts enormous Reynolds numbers and highly turbulent conditions during the initial decent of the dispersed metal in a magma ocean, and laboratory experiments predict partial although incomplete equilibration between the silicate and metal components (Righter et al., 1997). Heuristic considerations (Rubie et al., 2003) and calculations (Sasaki and Abe, 2007) indicate that large metal masses are likely to be unstable in a

* Corresponding author.
E-mail address: cking44@jhu.edu (C. King).

0012-821X/$ – see front matter © 2011 Elsevier B.V. All rights reserved.
doi:10.1016/j.epsl.2011.02.037

magma ocean and will tend to break up, forming smaller droplets during free fall. Once the metal free fall phase is over, further approach to chemical equilibrium becomes more problematic. A key unanswered question for chemical equilibration is what fraction of the metal becomes dispersed into small droplets and what fraction remains in the form of larger masses. We assume the equilibration process occurs solely in the magma ocean and therefore only the dispersed metal droplets and not the large metal masses become equilibrated. This is clearly an over simplification, but allows us to apply geochemical constraints to our model. We further assume that dispersed metal droplets gradually rain to the bottom of the magma ocean, entering the conduits that trail the diapirs formed by the larger masses of the remnant impactor proto-cores (Karato and Murthy, 1997; Ricard et al., 2009; Ziethe and Spohn, 2007).

Although it is possible that the entire silicate mantle could have been molten at times (Solomatov, 2000; Tonks and Melosh, 1993), evidence suggests it is unlikely that the metal now in the core equilibrated within a totally molten mantle. First, the solidification time scales of a totally molten mantle are likely very short. According to thermal history calculations, deep magma oceans would solidify in $10^3 - 10^5$ years, whereas a shallow magma ocean could persist in the upper mantle up to 10^8 years, depending on the radiative thickness of its atmosphere (Solomatov, 2000). Second, the abundances of moderately siderophile elements in the present day mantle suggest equilibration pressures and temperatures that place the base of a magma ocean at mid-mantle or upper-mantle depths. Ni, Co, V, Cr, Si and Nb are all found in higher abundances in the mantle than predicted for near-surface equilibration, because these elements strongly partition into metal at low pressure (Rubie et al., 2007). Specifically equilibration between Fe–Ni–S-alloy and liquid silicate at present day depths near 1200 km or pressure lower than 30 GPa explains the Ni and Co abundances in the mantle today (Righter and Drake, 2001; Wood et al., 2006), and mantle V, Cr, Si, and Nb abundances constrain the temperature of equilibration to a temperature above 2400 K and below 4200 K (Li and Agee, 2001).

In addition to temperature and depth, siderophile element abundances also constrain how much chemical equilibration the metal and silicate experienced prior to final core segregation. According to Rudge et al. (2010), about 36% of the metal equilibrated with the silicate mantle prior to the end of core formation, and according to Sasaki and Abe (2007), as much as 20% equilibrated during each large impact. These percentages could be interpreted as the mass fraction of metal dispersed into droplets by impact and mixing processes. What was the form of the remaining metal? Fluid dynamical models of core formation have shown that coherent masses of liquid metal tend to form nearly or partially spherical diapirs, through Rayleigh–Taylor instabilities and other mechanisms (Monteux et al., 2009; Olson and Weeraratne, 2008; Sasaki and Abe, 2007; Walter and Tronnes, 2004). There is limited possibility for such large metal diapirs to equilibrate in the deep mantle. Diapirs can increase the temperature in the surrounding silicate by viscous dissipation, possibly enough for melting, which would increase the chemical diffusivity and somewhat accelerate chemical equilibration (Samuel and Tackley, 2008). However, the degree of chemical equilibration has been shown to be minimal in large diapirs (Samuel et al., 2010) and is expected to be negligible in comparison with the equilibration between metal droplets and silicate melt in a magma ocean.

The thermal state of the present day Earth in the core–mantle boundary (CMB) region offers constraints on the degree of thermal equilibration between core-forming metals and mantle silicates during core formation. Today there is an intrinsic temperature difference of 1000–2000 K across the D" layer separating the adiabatic portion of the lower mantle from the outer core (Anderson, 2002; Buffett, 2003). Adiabatic extrapolation of the 4100 K temperature estimate for the outer core at the CMB to surface pressure indicates the core now has +1000 K of superheat (potential temperature relative to surface melting temperature), whereas the present day mantle has far less superheat (Nimmo, 2007). In other words, the present day thermal disequilibrium of the core and mantle is about as great as their chemical disequilibrium was during Earth formation, in spite of the fact that chemical diffusion is far slower than thermal diffusion. The present day superheat of the core could be a consequence of heat sources in the core. Possible heat sources for superheating the core after its formation include radioactive decay of ^{40}K, ohmic and viscous heating. However, none of these is large enough to compensate for the secular cooling of the core over time. More plausibly, core superheat is a relic of the core formation process (Golabek et al., 2009; Ke and Solomatov, 2009). Energy sources available to heat the core during its formation include shock wave heating derived from the kinetic energy of impacts (Arkani-Hamed and Olson, 2010) and the change in potential energy to thermal energy via viscous dissipation as metal descends through the mantle (Monteux et al., 2009).

There are many proposed mechanisms for core formation, but only some of these preferentially heat the core. Metal percolation is possible in planetesimals and under high pressures due to small dihedral angles (Shannon and Agee, 1998; Yoshino et al., 2003), however, this mechanism does not increase the core's temperature preferentially, as the heat produced by percolation is dispersed throughout the mantle. Metal from the projectile could also directly merge with the proto-core if the projectiles were large enough to produce a magma ocean that extended to the CMB (Tonks and Melosh, 1993). Merging of cores through an entirely molten mantle is not considered here because the heat absorbed by merging cores is hard to quantify, the likelihood that the entire Earth was repeatedly liquified by impacts seems remote, and finally, this mechanism does not allow for any post-accretion equilibration of metal and silicate.

In this paper we argue that the same dynamical process of core formation that controls core–mantle chemical equilibrium also controls the core superheat. Specifically, we propose a segregation process that includes both metal diapirs and metal droplets in metal-silicate plumes allowing for partial chemical equilibration and producing a superheated post-accretion core. Consistent with the standard accretion model, we assume that large impacts create transient magma oceans on the growing Earth. Some of the metal from each impacting projectile sinks to the bottom of the magma ocean and through the solid mantle in large liquid diapirs, while the remainder is dispersed in smaller masses, assumed here to be droplets. The relative proportion of large metal masses to small metal droplets is a model parameter and is assumed to have the same value for all impacts.

Previous studies come to different conclusions about the heat supplied to the core by large diapirs (Monteux et al., 2009; Samuel et al., 2010), but the general consensus is that much of their viscous heating remains in the mantle due to the large viscosity difference between the liquid metal diapir and solid silicate mantle. Accordingly, the diapirs in this study are assumed to experience only adiabatic increases in temperature during their decent. We further assume that the dispersed metal descends from the magma ocean to the growing core within liquid metal-silicate conduits, consisting of superheated silicate melt and superheated metal droplets. Superheating in the conduits occurs as the potential energy of the droplets is converted to heat by viscous dissipation, which is localized within the narrow conduits. Only a portion of this localized viscous heating is lost by conduction into the solid silicate mantle, so the metal droplets are superheated as they enter the growing core. A similar model was proposed by Ke and Solomatov (2009) through which a low-viscosity iron diapir mostly dissipating heat in the mantle, whereas iron sinking through the mantle in a channel preferentially heats the iron. Like Ke and Solomatov (2009) we find that heat partitioning depends on the structure of the descending iron, and we also consider heat and mass exchange between metal-silicate conduit and the mantle.

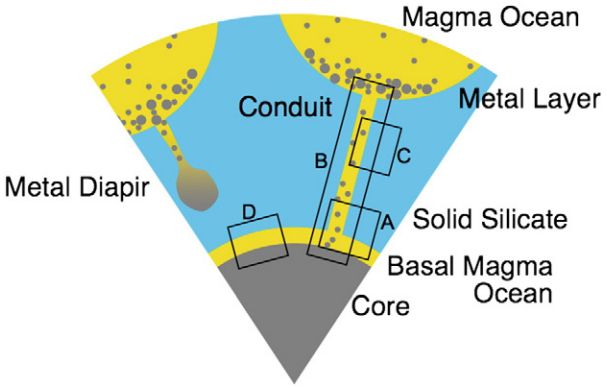

Fig. 1. Cross section sketch of accreting Earth showing the differentiation structures assumed in our model. Silicate melt represented in yellow, solid silicate represented in blue and liquid iron represented in gray. Control volumes outlined by boxes A, B, C and D are shown in Fig. 2.

2. Model

Fig. 1 is an illustration of the core formation model just described that includes both metal diapirs and droplets. It shows in cross section two liquid magma oceans formed by giant impacts, the solid silicate mantle, and the growing liquid metal core. All impacts in this study are assumed to be large enough to create at least a local magma ocean (Labrosse et al., 2007). Each impact is assumed to have the same characteristics except for its size. We assume that shock heating produces the same temperature anomalies for metal and silicate, i.e. any initial pre-impact heat anomaly is erased by the impact, resulting in a uniform temperature in the magma ocean. Metal dispersed in the magma ocean following impact events is shown as spherical droplets. It does not show the remnant impactor core descending in the magma ocean, but rather illustrates an already formed diapir in the solid mantle. As this diapir descends through the solid mantle, it remains connected to the near-surface magma ocean via a narrow conduit that consists of a mixture of liquid silicate and liquid metal droplets from the magma ocean (Olson and Weeraratne, 2008). On the right of Fig. 1 is a fully developed conduit with a mixture of liquid silicate and metal droplets that connects the near-surface magma ocean to a basal magma ocean and the growing core.

Assuming that low viscosity metal diapirs descend through the high viscosity solid mantle by Stokes flow, much of their gravitational potential energy released is deposited as heat by viscous dissipation in the surrounding mantle (Ke and Solomatov, 2009). The diapir absorbs only a small fraction of the heat its decent generates and never approaches thermal equilibrium with the surrounding mantle, because the thermal equilibration time of a large diapir is longer than its time of decent. Accordingly, the average temperature in the diapir increases approximately adiabatically with depth. In our model, this metal component is assumed to add an adiabatic increase to the temperature of the growing core.

In contrast, the thermal equilibration time of the small metal droplets is short compared to their time of decent through the conduit, and the viscosity of the metal and silicate liquids are not grossly different. Under these conditions, dispersed metal is nearly in local thermal equilibrium with molten silicates throughout the conduit. In addition, the viscous dissipation caused by the falling metal droplets and the rising silicate liquid is concentrated within the conduit, so that the heat produced by the release of gravitational potential energy of the falling droplets is also concentrated in the conduit. In our model, we assume that all of the heat produced by falling droplets is generated within the conduit, that the falling droplets are in local thermal equilibrium with the silicate melt in the conduit, and that the droplets contribute all of their heat, including their superheat, directly into the core as they cross the CMB. Let f denote the fraction of metal in each impact that descends to the core in the form of large diapirs, so that $1-f$ represents the metal fraction that sinks to the core as droplets within the conduit. Because metal superheating takes

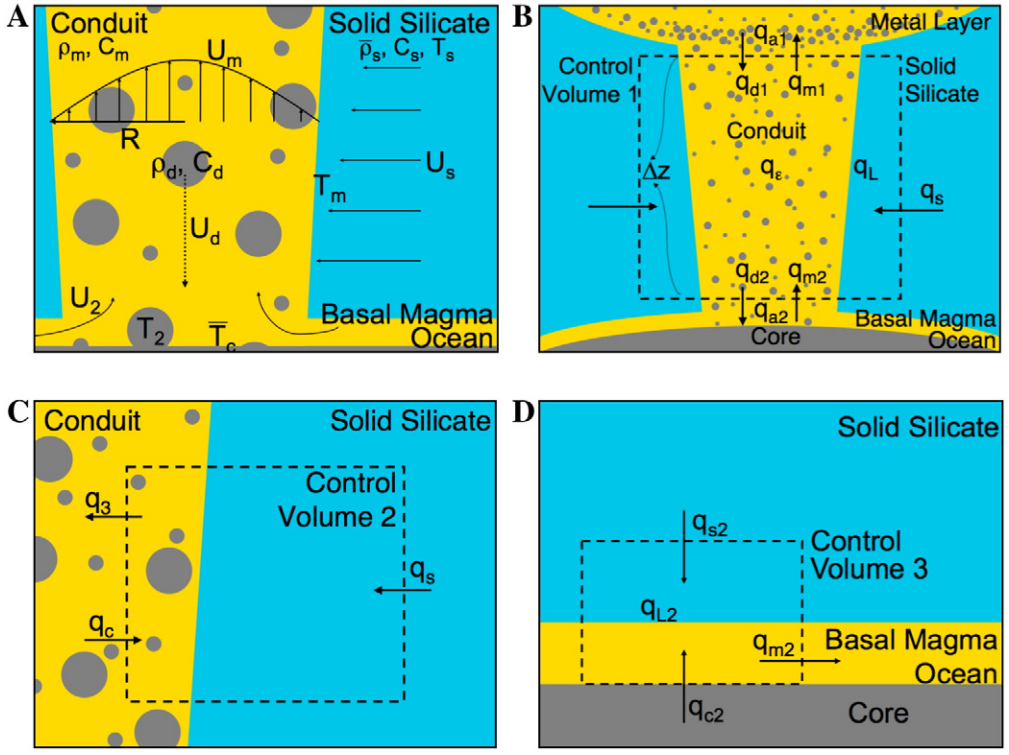

Fig. 2. Details of 3 control volumes shown in Fig. 1. Sketch A shows the motions in a metal–silicate conduit connected to the basal magma ocean. Conduit flow consists of silicate melt in an ascending Poiseuille flow plus descending metal droplets. Panel B shows an entire conduit and defines control volume CV1. Panel C defines control volume CV2 and the terms that contribute to its heat balance, including the entrained silicate mantle. Panel D defines the third control volume CV3.

place only within the conduits in our model, the amount of core superheating depends inversely on f.

Fig. 2 is an illustration of the structure and physical properties of the model. Fig. 2A is the lower portion of a fully developed conduit of radius R and shows a basal magma ocean produced by contact with the superheated, growing core. Velocities U_d of the metal droplets in gray are indicated by dashed arrows, the vertical velocity U_m of the silicate melt in the conduit, the inflow velocity U_2 of the basal magma ocean and the horizontal entrained solid mantle velocity U_s are all indicated by solid arrows. Temperature along the wall of the conduit is maintained at the eutectic melting temperature of the mantle T_m, dependent on pressure. The metal droplets leave the conduit at an average temperature T_2. The average temperature of the core is $\overline{T_c}$ and the surrounding solid silicate mantle temperature is T_s. The densities of the silicate melt, solid silicate mantle, and metal droplets are ρ_m, $\overline{\rho_s}$ and ρ_d, respectively. Specific heat of the silicate melt, solid silicate mantle and metal droplets are C_m, C_s, and C_d, respectively. Their nominal values, as well as other parameters, are listed in Table 1. With the release of potential energy of the droplets, the temperature of the conduit increases with depth due to viscous dissipation faster than the adiabat. Some of the superheat in the conduit is conducted into the solid silicate mantle, melting the conduit wall and entraining horizontally the newly formed melt, which then rises in the conduit as a Poiseuille flow. The entrainment of molten mantle material produces a conduit radius that increases with distance from the CMB to the base of the magma ocean.

Fig. 2B is a diagram of an already established conduit transporting metal to the growing core and connecting a shallow magma ocean to the basal magma ocean. As the silicate mantle grows, the height of the conduit Δz increases. The terms contributing to the heat balance in control volume 1 (CV1) are labeled as q. Positive contributions to the heat balance include the heat content of the droplets entering the control volume q_{d1}, the heat content from solid silicate mantle entrainment q_s, the heat content of silicate melt entering the control volume from the basal magma ocean q_{m2}, the adiabatic increases due to pressure $q_{a1}-q_{a2}$, and viscous dissipation of the descending droplets q_ϵ. The heat losses from the control volume include the heat content of the droplets leaving the control volume q_{d2}, the heat content of silicate melt leaving the control volume entering the shallow magma ocean q_{m1} and the latent heat released from the melting of the solid silicate mantle entrainment q_L. This control volume extends into the solid silicate. Therefore, entraining silicate is solid along the sides, and liquid when leaving and entering the conduit. This is an oversimplification as it ignores the difference between solidus and liquidus of the mantle.

Fig. 2C is a cross section of a conduit transporting metal droplets toward the growing core and silicate melt toward the shallow magma ocean. The control volume 2 (CV2) extends from inside the conduit into the solid silicate mantle. Positive heat contributions to CV2 include the heat content from solid silicate mantle entrainment q_s, and the heat conducted across the conduit wall q_c. The heat lost from CV2 includes the heat content entering the conduit but leaving CV2 as silicate melt, labeled q_3. We assume that the melt at the CMB is positively buoyant, although some other studies suggest otherwise (Labrosse et al., 2007). Whether the basal magma ocean is buoyant or not only affects the conduit fluxes in our model, and only nominally affects the core temperature.

Fig. 2D is an illustration of the lower mantle entrained into a basal magma ocean above the growing metal core, and shows control volume 3 (CV3). The positive contributions to the heat balance in CV3 include the heat content of the entrained solid silicate mantle q_{s2} and the heat conducted across the CMB q_{c2}. The heat loses from CV3 include the latent heat released from the melting of the basal magma ocean q_{L2}, and the ratio of heat leaving CV3 and entering CV1 q_{m2}. As the hot core conducts heat q_{c2} into the solid silicate mantle, the silicate mantle melts, forming a basal magma ocean. Due to its assumed positive buoyancy, the silicate melt from the base of the magma ocean travels along the CMB until it reaches the conduit, and results in heat q_{m2} leaving CV3. The silicate melt is replaced by solid silicate that slowly descends to the CMB. This entrained mantle heat q_{s2} enters the top of CV3. Melting occurs at the top of the basal magma ocean by entrainment of the solid mantle, producing a latent heat release q_{L2}. Parameters for control volumes are listed in Table 2.

The heat balance for control volume CV1 can be written in terms of the notation in Fig. 2 as

$$q_{d1}-q_{d2}+q_\epsilon-q_{m1}+q_{m2}-q_L+q_s+q_{a1}-q_{a2}=0, \tag{1}$$

the heat balance for control volume CV2 in terms of Fig. 2 notation is

$$q_c+q_s-q_3=0, \tag{2}$$

and the heat balance for control volume CV3 in terms of Fig. 2 notation is

$$q_{c2}+q_{s2}-q_{m2}-q_{L2}=0. \tag{3}$$

Using the model parameters listed in Table 1, Table 2 and Fig. 2, the various terms in Eq. (1) are given by

$$q_{d1}=F_{in}C_dT_{m1}\quad q_{d2}=F_{in}C_dT_2\quad q_\epsilon=\epsilon V_t \tag{4}$$

Table 1
Assumed values.

Symbol		Inputs	Assumed value	References[a]
α_c	$[K^{-1}]$	Thermal expansion coefficient of metal droplets	3×10^{-5}	1
α_m	$[K^{-1}]$	Thermal expansion coefficient of silicate melt	2×10^{-5}	1
β_d	$[GPa^{-1}]$	Compressibility coefficient of metal droplets	6×10^{-3}	2
β_m	$[GPa^{-1}]$	Compressibility coefficient of silicate melt	5.15×10^{-3}	3
T_{m1}	$[K]$	Average temperature at the base of the magma ocean	2854	
C_d	$[J\ kg^{-1}K^{-1}]$	Specific heat of the metal droplets	825	4
C_m	$[J\ kg^{-1}\ K^{-1}]$	Specific heat of the silicate melt	1000	5
C_s	$[J\ kg^{-1}\ K^{-1}]$	Specific heat of the solid silicate	1000	5
$\Delta\rho_s$	$[kg\ m^{-3}]$	Density difference between solid silicate and silicate melt	500	
G	$[m^3\ kg^{-1}\ s^{-2}]$	Gravitational constant	6.673×10^{-11}	
k	$[W\ m^{-1}\ K^{-1}]$	Thermal conductivity of silicate	4.2	6
L	$[J\ kg^{-1}]$	Latent heat coefficient of silicate	4×10^5	5
P_1	$[GPa]$	Pressure at the bottom of the shallow magma ocean	28	7
ρ_{d1}	$[kg\ m^{-3}]$	Density of metal droplets at the base of the magma ocean	7000	
ρ_{m1}	$[kg\ m^{-3}]$	Density of silicate melt at the base of the magma ocean	4000	
$\overline{\rho_s}$	$[kg\ m^{-3}]$	Average density of solid silicate	4500	
$\overline{\rho_c}$	$[kg\ m^{-3}]$	Average density of core	10,667	

[a] References: 1 Reese and Solomatov (2010), 2 Hayward (1971), 3 Turcotte and Schubert (2002), 4 Beutl et al. (1994), 5 Rubie et al. (2003), 6 Farnetani and Hofmann (2009), 7 Solomatov (2000).

Table 2
Variable list.

Symbol		Definition
A_*	$[m^2]$	Cross sectional conduit area
A_s	$[m^2]$	Conduit surface area
A_c	$[m^2]$	Core surface area
ϵ	$[W\ m^{-3}]$	viscous dissipation density
f		Metal fraction in diapir
F_{in}	$[kg\ s^{-1}]$	Metal influx into conduit
N		Number of impacts
Q_e	$[m^3\ s^{-1}]$	Volumetric side entrainment
q_3	$[W]$	Heat content entering the side of the conduit, exiting CV2
$q_{a1}-q_{a2}$	$[W]$	Adiabatic increase
q_c	$[W]$	Heat conducted across the conduit wall
q_{c2}	$[W]$	Heat conducted across the CMB
q_{d*}	$[W]$	Heat content of the metal droplets
q_ϵ	$[W]$	Viscous dissipation of the metal droplets
q_L	$[W]$	Latent heat released from melting of the entrainment around the conduit
q_{L2}	$[W]$	Latent heat released from melting of the entrainment around the core
q_{m*}	$[W]$	Heat content of the liquid silicate
q_s	$[W]$	Heat content from solid silicate mantle entrained into the conduit
q_{s2}	$[W]$	Heat content from the solid silicate mantle entrained owards the CMB
R	$[m]$	Conduit radius
r_c	$[m]$	Core radius
r_s	$[m]$	Radius of the surface of the Earth
T_*	$[K]$	Cross sectional average temperature of conduit
$\overline{T_c}$	$[K]$	Average core temperature
T_i	$[K]$	Average temperature of diapir
T_{m*}	$[K]$	Melting temperature of silicate, surface temperature of conduit
T_o	$[K]$	Maximum temperature of conduit cross section
$\overline{T_s}$	$[K]$	Average temperature of solid silicate
U_*	$[m\ s^{-1}]$	Vertical silicate melt velocity in conduit
U_A	$[m\ s^{-1}]$	Radial velocity of CMB
U_d	$[m\ s^{-1}]$	Terminal velocity of droplets
U_s	$[m\ s^{-1}]$	Entrained solid silicate velocity
V_t	$[m^3]$	Total conduit volume
Δz	$[m]$	Conduit height

*Depth dependent variable. A subscript 1 refers to the top of the conduit while a subscript 2 refers to the bottom of the conduit.

$$q_{m1} = \left(F_{in}\frac{\rho_{m1}}{\rho_{d1}} + Q_e\right)C_m T_{m1} \quad q_{m2} = F_{in}\frac{\rho_{m1}}{\rho_{d1}}C_m\frac{T_{m2}+\overline{T_c}}{2} \tag{5}$$

$$q_L = Q_e L \quad q_s = Q_e C_s \overline{T_s} \tag{6}$$

$$q_{a1} = A_1 U_1 \alpha_m T_{m1} P_1 \quad q_{a2} = A_2 U_2 \alpha_m \frac{T_{m2}+\overline{T_c}}{2} P_2 \tag{7}$$

where F_{in} is the metal influx rate entering the control volume through the top of the conduit, T_{m1} is the melting temperature at the top of the conduit and CV1, ϵ is the viscous dissipation density, V_t is the total volume of the conduit, ρ_{m1} is the density of the silicate melt at the top of the conduit and CV1, ρ_{d1} is the density of the metal droplets at the top of the conduit and CV1, Q_e is the volumetric side entrainment of the solid silicate mantle, L is the latent heat coefficient of the silicate mantle, $\overline{T_s}$ is the average temperature of the solid silicate mantle, A_1U_1 is the volumetric flow rate of the silicate melt through the top of the conduit, α_m is the thermal expansion coefficient of the silicate melt, P_1 is the pressure at the top of the conduit and CV1, A_2U_2 is the volumetric flow rate of the silicate entering CV1 from the basal magma ocean, T_{m2} is the melting temperature of the eutectic composition of the mantle at the bottom of CV1 above the CMB, and P_2 is the pressure at the bottom of CV1 above the CMB.

Similarly, using the model parameters in Table 1, Table 2 and Fig. 2, the terms in Eq. (2) are given by

$$q_c = \frac{2k(T_o - T_m)A_s}{R} \quad q_3 = Q_e C_s \overline{T_m} \tag{8}$$

where k is the thermal conductivity of the solid silicate mantle, T_o is the maximum temperature in the conduit at a specific depth, A_s is the surface area of the conduit proportional to R, and $\overline{T_m}$ is the average vertical melting temperature along the wall of the conduit. In the same way, the terms in Eq. (3) are given by

$$q_{c2} = q_{m2} - q_{s2} + q_{L2} \quad q_{s2} = F_{in}\frac{\rho_{m1}}{\rho_{d1}}C_m\overline{T_s} \quad q_{L2} = F_{in}\frac{\rho_{m1}}{\rho_{d1}}L \tag{9}$$

The analysis requires an additional control volume surrounding the growing core, its surface defined by the moving CMB, denoted by the control volume 4 (CV4). For this control volume the heat balance can be written as

$$C_d\overline{\rho_c}\int_V \frac{\partial T}{\partial t}dV + C_d\overline{\rho_c}\int dA\cdot U_A\overline{T_c} - \int_V \alpha_c\overline{T_c}\frac{dP}{dt}dV + \int_A (q_{cond} - q_{conv})\cdot dA = 0 \tag{10}$$

where $\overline{\rho_c}$ is the mean density of the core, $\frac{1}{V}\int_V \frac{\partial T}{\partial t}dV$ is the volumetric average rate of change of temperature also written as $\dot{T}_c$, A_c is the surface area of the CMB modeled as a sphere, and U_A is the radial velocity of the expanding CMB. In terms of the model parameters listed in Table 1, Table 2 and Fig. 2, the various terms in Eq. (10) are defined as

$$C_d\overline{\rho_c}\int dA\cdot U_A\overline{T_c} = C_d\overline{\rho_c}\frac{F_{in}\overline{T_c}}{\rho_{d2}} \quad \int_A q_{cond}\cdot dA = q_{c2} \quad \int_A q_{conv}\cdot dA = q_{d2} \tag{11}$$

$$\int_V \alpha_c\overline{T_c}\frac{dP}{dt}dV = \frac{8\pi^2 G\overline{\rho_c}^3\alpha_c\overline{T_c}\left(r_{c2}^5 - r_{c1}^5\right)}{15(t_2 - t_1)} \tag{12}$$

where ρ_{d2} is the density of the metal droplets at the bottom of CV1 entering CV4, α_c is the thermal expansion coefficient of the core, G is the gravitational constant, r_{c2} is the core's radius at t_2, r_{c1} is the core's radius at t_1, t_1 and t_2 are two sequential time steps. In writing Eq. (12) the term dP/dt has been approximated by finite differencing of the hydrostatic pressure evaluated at time t_2 and t_1. The system of five Eqs. (1), (2), (3), (10) and (12), can be solved for the five unknowns T, R, $\overline{T_c}$, q_{c2} and $\dot{T}_c$ as a function of time, once the accretion history $F_{in}(t)$ is specified.

The first term in Eq. (10) can be re-written in finite difference form to give the change in average core temperature from one time step to the next

$$\overline{T_c}(t_2) \simeq \overline{T_c}(t_1) + \dot{T}_c\Delta t \tag{13}$$

where $\Delta t = t_2 - t_1$. This equation is for growth of the core by a conduit. In between the successive conduits, diapirs are the source of heating and mass addition to the core. For diapirs, the temperature change of the core can be calculated as follows

$$\overline{T_c}(t_2) = \frac{\overline{T_c}(t_1)r_{c1}^3 + T_i\left(r_{c2}^3 - r_{c1}^3\right)}{r_{c2}^3} \tag{14}$$

In terms of the model parameters in Tables 1, 2 and Fig. 2, T_i, the temperature of the diapir entering the core is defined as

$$T_i = T_{m1} + \alpha_c \frac{T_{m1} g \Delta z}{C_d} \tag{15}$$

where g is the average gravitational acceleration in the mantle.

For several of the parameters in the model, the values change with the size and differentiation of the Earth. The Earth's surface radius r_s and core radius r_c grow with material added by each impact. The Earth's core radius growth rate has an additional dependence on the fraction f of metal material partitioned into diapirs and the metal influx rate into the conduit F_{in}. The radial velocity of the CMB is given by

$$U_A = \frac{F_{in}}{\rho_{d2} A_c} \tag{16}$$

where A_c is the surface area of the core. The height of the conduit, Δz, the distance between the shallow magma ocean and the growing core, is given by

$$\Delta z = \left(r_s - \frac{P_1}{\overline{\rho_s} g}\right) - r_c \tag{17}$$

where P_1 is the pressure at the top of the conduit and CV1. Average gravity in the mantle is also dependent upon the size of the silicate mantle. Based on the parameters in the above equations, g can be written as

$$g = \frac{\frac{4\pi}{3} G \left(r_c^2 (\overline{\rho_c} - \overline{\rho_s}) - \frac{r_c^3}{r_s} (\overline{\rho_c} - \overline{\rho_s}) + \frac{1}{2} \overline{\rho_s} r_c^2 \right)}{r_s - r_c} \tag{18}$$

whereas before r_s is the Earth's surface radius and r_c is the Earth's core radius at any time t.

The top cross sectional area of the conduit A_1 and outflow velocity U_1 as well as the bottom cross sectional area of the conduit A_2 and inflow velocity U_2 are also dependent on F_{in} as well as other previously defined parameters, according to

$$A_1 U_1 = \frac{F_{in}}{\rho_{d1}} + \frac{Q_e}{\rho_{m1}} \qquad A_2 U_2 = \frac{F_{in}}{\rho_{d1}} \frac{\rho_{m1}}{\rho_{m2}} \tag{19}$$

where $A_1 U_1$ is the volumetric outflow rate of the silicate melt from CV1 and $A_2 U_2$ is the volumetric inflow rate at the bottom of the conduit and CV1.

Physical properties dependent on pressure include the melting temperature T_m and ambient temperature of the solid silicate mantle T_s

$$T_m = -0.1301 P^2 + 34.907 P + 1978.9 \quad T_s = 6.1111 P + 1755.56 \tag{20}$$

where P is pressure in GPa and both T_m and T_s are in K. This liquidus estimate is based on a eutectic composition of MgO and PV (Boehler and Ross, 2007). The temperatures in the solid silicate are based on the mantle adiabat (Turcotte and Schubert, 2002). The density of the silicate melt and metal droplets also depend on pressure and are given by

$$\rho_m = 4000(1 + \beta_m (P - P_1) - \alpha_m (T - T_{m1})) \tag{21}$$
$$\rho_d = 7000(1 + \beta_d (P - P_1) - \alpha_d (T - T_{m1}))$$

where β_m is the compressibility coefficient for silicate melt, β_d is the compressibility coefficient of the metal droplets and T is the average temperature in the conduit at depth z. In Eq. (21), the units of ρ_m and ρ_d are $kg\ m^{-3}$, P and P_1 are GPa, T and T_{m1} are K, β_m and β_d are GPa^{-1} and α_m and α_d are K^{-1}.

Some of the heat terms in Eqs. (1), (6), and (8) are also dependent on the height of the conduit. In particular the viscous dissipation of the descending droplets q_ϵ and the volumetric side entrainment of the solid silicate mantle Q_e can be written in terms of the changing Earth radius and consequently the changing Δz. Specifically ϵ, V_t and Q_e can be written in terms of previously defined variables in Fig. 2 and Eqs. (6), (4) and (8), simplifying q_ϵ and Q_e to

$$q_\epsilon = F_{in} g \int_{z_2}^{z_1} \frac{\Delta \rho_d}{\rho_d} dz \tag{22}$$

$$Q_e = \frac{4\pi k \int_{z_2}^{z_1} (T_o - T_m) dz}{C_s (\overline{T_m - T_s})} \tag{23}$$

where $\Delta\rho_d = \rho_d - \rho_m$ at depth z, z_2 corresponds to the depth at the base of the conduit at the CMB, z_1 corresponds to the depth at the top of the conduit, and $\overline{T_m - T_s}$ is the average difference between the melting temperature and solid silicate temperature over the entire conduit height. The maximum temperature in a cross section of the conduit T_o is defined as

$$T_o = 2T - T_m \tag{24}$$

for any depth z. Metal and silicate liquid viscosities are not important in this study as they cancel from our final equations, provided that the metal and silicate liquids have similar viscosities that are much smaller than the viscosity of the solid silicate.

3. Results

We have examined three proposed histories of Earth accretion and differentiation. Each accretion history starts with a proto-Earth that has 16.7% of the current Earth volume, an initial mass of 10^{24} Kg and 31.6% of its mass in its liquid metallic core. Although, the proto-Earth was most likely always dominated by large impacts during formation, our study begins with the magma ocean with its deepest extent reaching just above the core–mantle boundary. This means that metal from subsequent impactors must sink through at least some of the solid silicate, and our diapir conduit model is applicable. For this initial condition, the average core temperature is set to 3103 K, the melting temperature of the eutectic composition ofthe silicate mantle at the 37.4 GPa, the initial pressure of the CMB, as given by (20). Each type of accretion history consists of a sequence of impacts, with every impact forming a large liquid metal diapir and narrow liquid metal silicate conduit. Every impact has the same fraction of silicate and metal with 31.6% metal by mass. We model the impacts as occurring in succession over 30 Ma, one after another with all the metal descending to the core before the next impact occurs, although in reality it is likely that impact distribution would not have been spaced evenly over the accretion time. The three accretion histories are designated as type I, for which the impactors are all the same size; type M, in which all the impactors are the same size except for the last roughly Mars-sized impact having a mass of 6.204×10^{23} Kg; and the third type E, for which the impactors decrease in size exponentially over the sequence until the last impact, which is again Mars-sized. For each type of history we consider the number of impacts N varying from 8 to 90 and the fraction of metal descending in each diapir f varying from 0 to 1.

Fig. 3 shows the growth of the Earth as well as the average temperature during the three types of accretion histories. For all results shown in Fig. 3, the metal fraction in each diapir is $f = 0.64$. Figure eftimedepA shows the radius of the surface of the Earth as a function of time for the case of 20 impacts. 20 impacts were chosen because similar results were found in cases with more impacts. With more impacts the time dependent curves for temperature and radius are smoothed, however, post-accretion average core temperatures remain similar. The growth history is in steps, the vertical steps representing impacts and

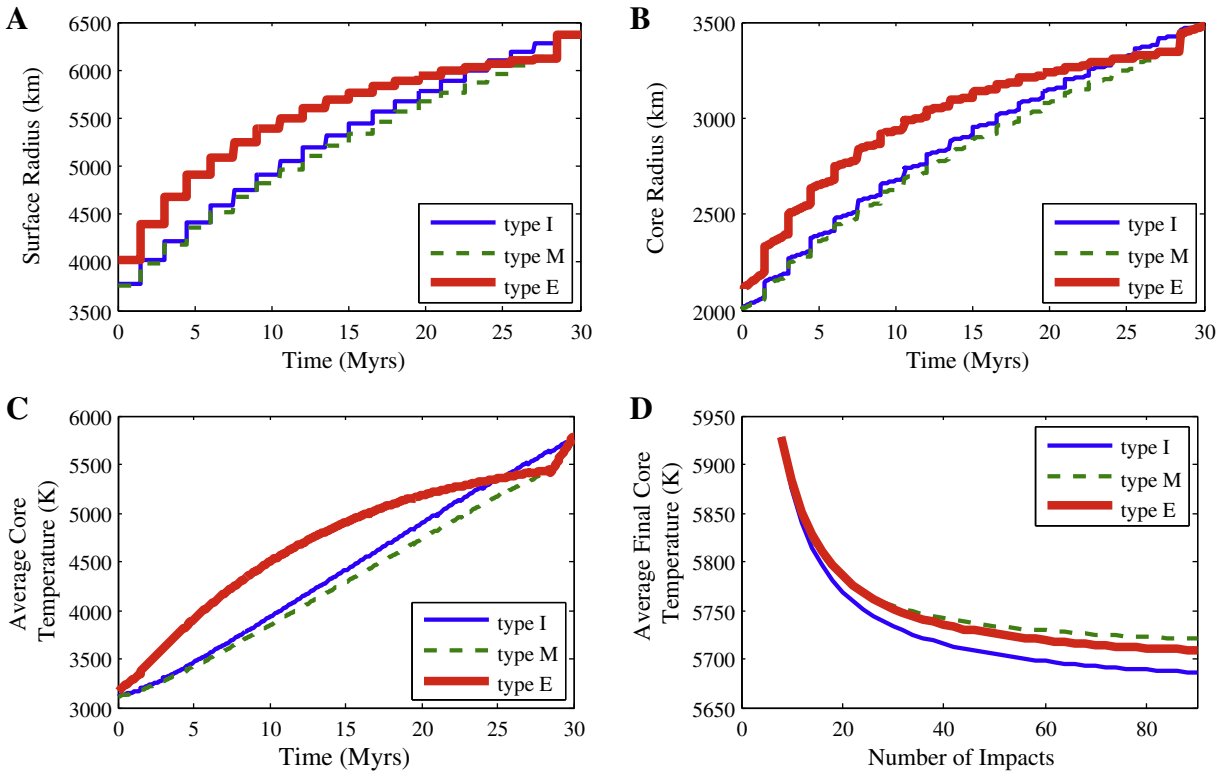

Fig. 3. Model accretion histories. In panels A–D the accretion history types I, type M, and type E are displayed as a thin solid line, a dashed line and a thick solid line, respectively, for the case of N = 20 and $f = 0.64$. Panel A shows the Earth's surface radius as a function of time. Panel B shows the radius of the core as a function of time. Panel C shows the average core temperature as a function of time. Panel D shows the post-accretion average core temperature as a function of the number of impacts.

the horizontal steps representing the time between impacts. Fig. 3B shows the radius of the core as a function of time for the same 20 impacts. In this figure the vertical steps represent diapirs added to the core and the sub-horizontal steps represent the addition to the core by metal droplets through conduits. Fig. 3C shows the three corresponding thermal histories of the core, here the average core temperature is plotted versus time. The small difference in starting temperature in the three accretion histories is due to the different sizes of the first impact. Accretion history types I and M follow similar trends throughout the accretion, whereas type E deviates from these two, with a higher temperature during the early stages. These trends are similar to the growth histories in Figs. 3A and B. Although the three accretion types have distinct thermal histories, their post-accretion core temperatures are nearly the same, shown in Fig. 3C and Table 3. Fig. 3D shows the post-accretion average core temperature as a function of number of impacts N for each accretion type. Post-accretion core temperature varies inversely with N, so that with fewer large impacts, each type of history results in a higher post-accretion average core temperature. The reason for this trend is that, with fewer large impacts, relatively less heat is diffused into the mantle, compared to the heat diffused into the mantle by many small impacts.

Fig. 4 shows the post-accretion average core temperature as a function of N and f. Fig. 4A shows results for type I accretion histories, corresponding to the thin line in Fig. 3. Generally the highest post-accretion core temperatures correspond to the smallest values of f, with the maximum post-accretion average core temperature of 8000 K corresponding to N = 8 impacts. The minimum post-accretion average core temperature is found to be 4000 K for $f = 1$ and N = 90 impacts. Overall, the post-accretion core temperatures decrease as N and f increase. Fig. 4B shows the difference in post-accretion average core temperatures between accretion types I and M, for otherwise identical N and f values. Temperature differences are shown here because the absolute temperatures of type M are very close to type I, as shown in Fig. 4A. The post-accretion temperature differences range from −65 to −10 K, demonstrating that accretion type M results in a slightly higher post-accretion core temperature than type I. Fig. 4C shows the difference in post-accretion average core temperature between accretion type I and E. Again, difference in temperature is

Table 3
Output values.

Outputs	Notation	Units	Case I	Case M	Case E
Initial core temperature	$\overline{T_{ci}}$	K	3103	3103	3103
Number of impacts	N		20	20	20
Fraction in diapir	f		0.64	0.64	0.64
Metal flux	F_{in}	$kg\ s^{-1}$	5.97×10^{8}	5.50×10^{8}, 1.49×10^{9}	$1.77\times10^{8}-1.58\times10^{9}$
Total of viscous dissipation	$\sum q_v \Delta t$	J	3.11×10^{30}	3.13×10^{30}	3.16×10^{30}
Efficiency	e		0.59	0.59	0.58
Final core temperature	$\overline{T_c}$	K	5770	5780	5790

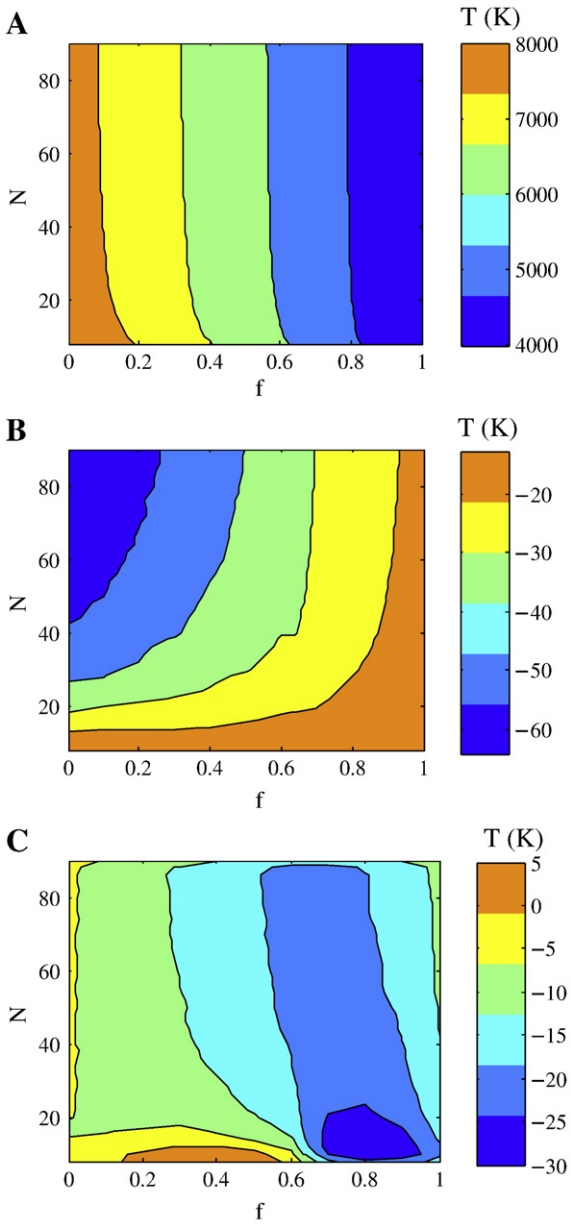

Fig. 4. Model post-accretion average core temperatures versus number of impacts N and diapir fraction *f*. Panel A shows the post-accretion average core temperature $\overline{T}_c$ for type I accretion history. Panel B shows the difference in $\overline{T}_c$ between type I and M accretion histories. Panel C shows the difference in $\overline{T}_c$ between type I and E accretion histories.

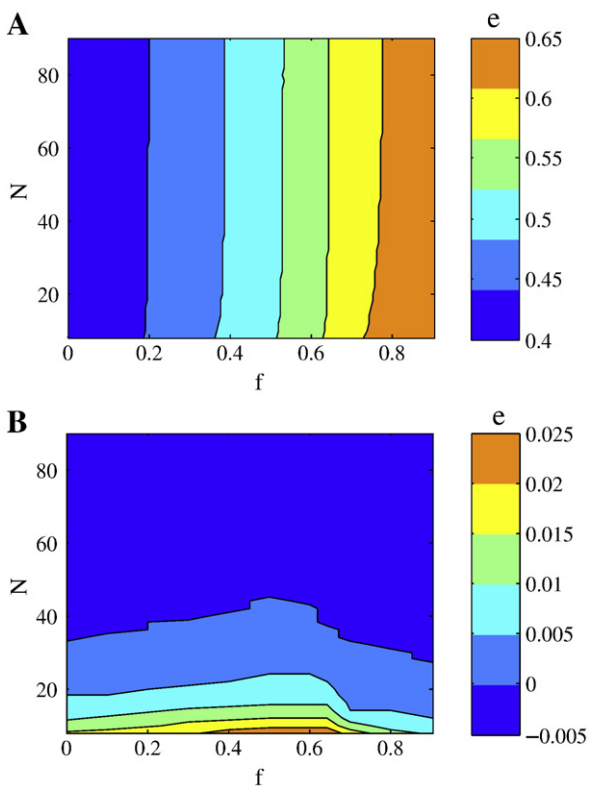

Fig. 5. Conduit efficiency as a function of N and *f*. Panel A shows the conduit efficiency of types I and M accretion histories. Panel B shows the differences in conduit efficiency between type I and type E accretion histories.

shown because the absolute temperatures of type E are very similar to type I. The temperature differences range from −30 to 5 K; furthermore, Fig. 4C shows that most of the temperatures of typeE histories are greater than type I. However, there are a few cases between $f=0.1$ and $f=0.6$ and for N<12 where type I produces a slightly hotter post-accretion core then type E.

Fig. 5 shows the conduit efficiency e in the three accretion histories as a function of N and *f*. Here, the conduit efficiency is defined as the total heating of the core by the conduits normalized to the heat available to the droplets from their change in gravitational potential energy over the entire accretion history. The efficiency defined this way can be written in terms of variables in Fig. 2 and Table 2 as

$$e = \frac{q^*_{d2} - q_{c2}}{q_{d1} + q_\epsilon} \tag{25}$$

where q^*_{d2} is the heat content of the droplets entering CV4 and core, with volume expansion and adiabatic effects removed. An efficiency of $e=1$ corresponds to conduits and core that are completely insulated, so that all the heat production goes into heating the core. Alternatively, $e=0$ corresponds to all the heat production by the metal droplets deposited in the mantle. According to (25), $e=0$ if all the metal in each impact is partitioned into the diapirs, because there is no viscous dissipation in the conduits. It is important to note that as *f* increases the efficiency also increases, except for $f=1$; this is the opposite of the post-accretion average core temperature relation to *f* shown in Fig. 4A. The maximum efficiency found for all three accretion types is $e=0.68$ at $f=0.9$ and $N=8$. Purely adiabatic core growth or $f=1$ is not displayed, as the efficiency of the conduits is $e=0$ for this case. As *f* increases due to more metal partitioning into the diapirs, the conduit radius, *R*, and the metal flux into the conduit, F_{in}, are reduced as is the amount of conduction into the solid mantle through the conduit. This effect is due to the smaller conduit surface area and smaller temperature difference between the conduit and solid silicate mantle. A decrease in heat conduction into the solid mantle by the conduits therefore increases the efficiency. The minimum efficiency is found to be $e=0.42$ for all three accretion histories when $f=0$ and $N=8$. The difference in conduit efficiencies between accretion type I and M are numerically insignificant, therefore Fig. 5A represents the efficiency for both types I and M. The efficiency difference is shown in Fig. 5B between accretion types I and E because the absolute efficiencies of type E are very similar to type I for otherwise identical N and *f* values. The differences in efficiency range from $e=-0.005$ to 0.025 and Fig. 5B shows that a majority of cases of type E are less efficient than type I, except for N greater than about 50.

4. Summary and discussion

Our model assumes Earth accretion and core differentiation occur simultaneously and the accretion history consists of a finite number of

impacts distributed over 30 Ma time, each impact large enough to create a regional or possibly global magma ocean. Our accretional histories incorporate two previously purposed modes of core differentiation: large metal diapirs and small metal droplets. Following an impact, the metal is distributed in large and small volumes. The metal droplets are small enough to equilibrate with the silicate in the magma ocean whereas, larger metal volumes form diapirs with enough negative buoyancy to sink through the solid mantle adiabatically. A narrow conduit trails the diapir, which remains molten due to the viscous dissipation of the descending metal droplets. We assume the droplets are small enough to thermally equilibrate with the viscous heating they produce, whereas the large diapirs do not. These basic assumptions are consistent with previous theoretical and experimental studies of metal-silicate separation processes (Monteux et al., 2009; Olson and Weeraratne, 2008; Samuel et al., 2010).

Considering different ratios of the fraction of metal in each diapir per impact f, the number of impacts N and accretion histories, we find post-accretion average core temperatures range between 4000 K and 8000 K. Considerations of chemical equilibration constrain a preferred diapir to total metal content of the impacts of $f=0.64$, according to Rudge et al. (2010). Unless accretion histories only include a few large impacts, the ratio of f is the critical factor in determining the post-accretion average core temperature. As f is reduced decreasing the size of the diapirs, the post-accretion average core temperature increases. Our preferred model based on $f=0.64$ and 34 impacts that decrease in size exponentially, type E. For the preferred model, the core temperature starts out at 3103 K and the diapir temperatures start out at 2854 K, the melting temperature at the base of the magma ocean. In this model 34 impacts produce a post-accretion average core temperature of 5740 K, the mean value between the temperature produced by 8 impacts of 5900 K and that produced by 90 impacts of 5700 K. Comparing our accretion sequence to N-body simulations we find that both have a relativelysmall number of energetically significant impacts, with the largest mass flux in the beginning of accretion, tapering off to a few large impacts near the end (Nimmo and Agnor, 2006). Typically, N-body simulations produce a wider distribution of impact masses than we assume in this study. One possible extension would be to apply specific N-body growth histories to our model.

The conduit efficiency e defined as the ratio of the effective heating of the core by the conduits to the change in gravitational potential energy in the conduits, increases with f and therefore is inversely proportional to the post-accretion average core temperature. For our preferred model the mean efficiency is $e=0.59$. Assuming that the present day CMB and inner core boundary (ICB) temperatures are 4100 K and 5520 K, respectively (Nimmo, 2007) the average core temperature today is about 4720 K. Based on our preferred model, this implies that the core has cooled on average by 1020 K following its formation, similar to an estimate by Stevenson (2008) of 1000 K. This temperature decrease is equivalent to an average cooling rate of 225 K per billion years over the last 4.5 billion years, corresponding to an average of 11 TW of sensible heat during that time, within the 5–15 TW range for present-day CMB heat flow (Anderson, 2002; Buffett, 2003; Lay et al., 2008).

The initial core temperature also plays a limited role, because of the small initial volume. Initial core temperatures of 1000 K or 6000 K change the final core temperature only by -300 K and $+200$ K respectively. Perhaps our biggest assumption is that the shock heating produces the same temperature in both the metal and silicate in the impactor, and is close to the temperature of the magma ocean. For small impacts, Monteux et al. (2009) find that both metal and silicate heat by about the same amount, 140–1925 K depending on the target body size, consistent with our assumptions. However, for large impacts such as the moon-forming event, there could be preferential heating in the metal of several thousand degrees above the iron vaporization temperature (Canup, 2004). Our model does not consider this possible temperature difference between metal and silicate for the largest impacts. Clearly, this is a simplification and therefore, our model produces a minimum temperature constrained by impacts. Finally, the starting temperature of the impactors is assumed to be close to that of the magma ocean. If the impactors had a proto-core significantly hotter than the magma ocean, the additional heat would be carried by the descending diapirs. However, as our model illustrates in Fig. 3C, so much heating of accretion occurs in the later stages, that there is no requirement that planetismals already had superheated cores.

Our model predicts a post-accretion average core temperature that provides a reasonable starting point for its thermal evolution, and also makes predictions about the early tectonic style of the mantle. According to our model, what is left behind after the core has formed is a mostly solid silicate mantle with hot upwellings where the metal-silicate conduits were located, and in addition, a remnant basal magma ocean. These structures would be able to transfer either silicate melt from the remnant basal magma ocean (assuming the basal magma ocean is buoyant with respect to the metal-free mantle) or alternatively, thermal plumes like those proposed for hot spots today. Due to the absence of heating by metal droplets, it is expected that the conduits would quickly solidify and evolve into sub solidus thermal plumes extending from the remnant basal magma ocean to the near-surface. This model can be extended to incorporate alternative early planetary growth scenarios and could provide estimates for cooling rates and post-accretion temperatures for other planetary cores.

Acknowledgements

This research was supported by grant EAR-0909622 from the Geophysics Program of the National Science Foundation.

References

Albarede, F.V., 2009. Accretion history of the terrestrial planets and dynamic implications. Nature 461, 1227–1233.
Anderson, O.L., 2002. The power balance at the core-mantle boundary. Phys. Earth Planet. Int. 131, 1–17.
Arkani-Hamed, J., Olson, P., 2010. Giant impacts, core stratification, and failure of the Martian dynamo. J. Geophys. Res. 115, E07012. doi:10.1029/2010JE003579.
Beutl, M., Pottlacher, G., Jager, H., 1994. Thermophysical properties of liquid iron. Int. J. Thermo. 15, 1323–1331.
Boehler, R., Ross, M., 2007. Properties of rocks and minerals-high-pressure melting. In: Price, G.D., Schubert, G. (Eds.), Treatise on Geophysics, vol 2. Elsevier B.V, pp. 527–541. ch 18.
Buffett, B.A., 2003. The thermal state of Earth's core. Science 299, 1675–1677.
Canup, R.M., 2004. Simulations of a late lunar-forming impact. Icarus 168, 433–456. doi:10.1016/j.icarus.2003.09.028.
Corgne, A., Keshav, S., Wood, B.J., McDonough, W.F., Fei, W., 2008. Metal-silicate partitioning and constraints on core composition and oxygen fugacity during Earth accretion. Geochim. Cosmochim. Acta 72, 574–589.
Dahl, T.W., Stevenson, D.J., 2010. Turbulent mixing of metal and silicate during planet accretion and interpretation of the Hf–W chronometer. Earth Planet. Sci. Lett. 295, 177–186.
Farnetani, C.G., Hofmann, A.W., 2009. Dynamics and internal structure of a lower mantle plume conduit. Earth Planet. Sci. Lett. 282, 314–322.
Golabek, G.J., Gerya, T.V., Kaus, B.J.P., Ziethe, R., Tackley, P.J., 2009. Rheological controls on the terrestrial core formation mechanism. Geochem. Geophys. Geosyst. 10, 1–31 Q11007.
Halliday, A.N., 2008. A young Moon-forming giant impact at 70–110 Ma accompanied by late-staged mixing, core formation and degassing of the Earth. Phil. Trans. Roy. Soc. A 366, 4163–4181. doi:10.1098/rsta.2008.0209.
Halliday, A.N., Wood, B.J., 2007. The composition and major reservoirs of the Earth around the time of the moon-forming giant impact. In: Stevenson, D.J. (Ed.), Treatise on Geophysics, vol 9. Elsevier B.V, pp. 13–50. ch 2.
Hayward, A.T.J., 1971. Precise determination of the isothermal compressibility of mercury at 20°C and 192 bar. J. Phys. D Appl. Phys. 4, 951–955.
Höink, T., Schmalzl, J., Hansen, U., 2006. Dynamics of metal-silicate separation in a terrestrial magma ocean. Geochem. Geophys. Geosyst. 7, 1–24 Q09008.
Karato, S., Murthy, V.R., 1997. Core formation and chemical equilibrium in the Earth-I. Physical considerations. Phys. Earth Planet. Int. 100, 61–79.
Ke, Y., Solomatov, V.S., 2009. Coupled core-mantle thermal evolution of early Mars. J. Geophys. Res. 144, 1–12.
Labrosse, S., Hernlund, J.W., Coltice, N., 2007. A crystallizing dense magma ocean at the base of the Earth's mantle. Nature 450, 866–869.

Lay, T., Hernlund, J., Buffett, B.A., 2008. Core-mantle boundary heat flow. Nat. Geosci. 1, 25–30.
Li, J., Agee, C.B., 2001. The effect of pressure, temperature, oxygen fugacity and composition on partitioning of nickel and cobalt between liquid Fe–Ni–S alloy and liquid silicate: implications for the Earth's core formation. Geochim. Cosmochim. Acta 65, 1821–1832.
Monteux, J., Ricard, Y., Coltice, N., Dubuffet, F., Ulvrova, M., 2009. A model of metal-silicate separation on growing planets. Earth Planet. Sci. Lett. 287, 353–362.
Nimmo, F., 2007. Energetic of the core. In: Olson, P. (Ed.), Treatise on Geophysics, vol 8. Elsevier B.V, pp. 31–65. ch 2.
Nimmo, F., Agnor, C.B., 2006. Isotopic outcomes of N-body accretion simulations: constraints on equilibration processes during large impacts from Hf/W observations. Earth Planet. Sci. Lett. 243, 26–43.
Olson, P., Weeraratne, D., 2008. Experiments on metal–silicate plumes and core formation. Phil. Trans. Roy. Soc. A 366, 4253–4271. doi:10.1098/rsta.2008.0194.
Pahlevan, K., Stevenson, D.J., 2007. Equilibration in the aftermath of the lunar-forming giant impact. Earth Planet. Sci. Lett. 262, 438–449.
Reese, C.C., Solomatov, V.S., 2010. Early martian dynamo generation due to giant impacts. Icarus 207, 82–90.
Ricard, Y., Sramek, O., Dubuffet, F., 2009. A multi-pase model of runaway core-mantle segregation in embryos. Earth Planet. Sci. Lett. 284, 144–150.
Righter, K., Drake, M.J., 2001. Constraints on the depth of an early terrestrial magma ocean. Meteorit. Planet. Sci. 36, 173.
Righter, K., Drake, M.J., Yaxley, G., 1997. Prediction of siderophile element metal-silicate partition coefficients to 20 GPa and 2800°C: the effects of pressure, temperature, oxygen fugacity, and silicate and metallic melt compositions. Phys. Earth Planet. Int. 100, 115–134.
Rubie, D.C., Melosh, H.J., Reid, J.E., Liebske, C., Righter, K., 2003. Mechanisms of metal-silicate equilibration in the terrestrial magma ocean. Earth Planet. Sci. Lett. 205, 239–255.
Rubie, D.C., Nimmo, F., Melosh, H.J., 2007. Formation of Earth's core. In: Schubert, G. (Ed.), Treatise on Geophysics, vol 9. Elsevier B.V, pp. 51–90. ch 3.
Rudge, J.F., Kleine, T., Bourdon, B., 2010. Broad bounds on Earth's accretion and core formation constrained by geochemical models. Nat. Geosci. 3, 439–443.
Samuel, H., Tackley, P.J., 2008. Dynamics of core formation and equilibration by negative diapirism. Geochem. Geophys. Geosyst. 9, 1–15 Q06011.
Samuel, H., Tackley, P.J., Evonuk, M., 2010. Heat partitioning in terrestrial planets during core formation by negative diapirism. Earth Planet. Sci. Lett. 290, 13–19.
Sasaki, T., Abe, Y., 2007. Rayleigh–Taylor instability after giant impacts: imperfect equilibrium of the Hf–W system and its effect on the core formation age. Earth Planet. Space 59, 1035–1045.
Shannon, M.C., Agee, C.B., 1998. Percolation of core melts at lower mantle conditions. Science 280, 1059–1061.
Solomatov, V.S., 2000. Fluid dynamics of magma oceans. In: Canup, R., Righter, K. (Eds.), Origin of the Earth and Moon. Univ. Arizona Press, Tucson.
Stevenson, D.J., 2008. A planetary perspective on the deep Earth. Nature 451, 261–265.
Tonks, W.B., Melosh, H.J., 1993. Magma ocean formation due to giant impacts. J. Geophys. Res. 98, 5319–5333.
Turcotte, D.L., Schubert, G., 2002. Geodynamics, 2nd ed. Cambridge University Press, New York.
Walter, M.J., Tronnes, R.G., 2004. Early Earth differentiation. Earth Planet. Sci. Lett. 225, 253–269.
Wood, B.J., Walter, M.J., Wade, J., 2006. Accretion of the Earth and segregation of its core. Nature 441, 825–833.
Yoshino, T., Walter, M.J., Katsura, T., 2003. Core formation in planetesimals triggered by permeable flow. Nature 422, 154–157.
Ziethe, R., Spohn, T., 2007. Two-dimensional stokes flow around a heated cylinder: a possible application for diapirs in the mantle. J. Geophys. Res. 112, B09403. doi:10.1029/2006JB004789.